

See discussions, stats, and author profiles for this publication at: <https://www.researchgate.net/publication/259152697>

High-Pressure Synthesis, Crystal Structure, and Properties of $\text{In}_2\text{NiMnO}_6$ with Antiferromagnetic Order and Field-Induced Phase Transition

ARTICLE in INORGANIC CHEMISTRY · DECEMBER 2013

Impact Factor: 4.76 · DOI: 10.1021/ic401917h · Source: PubMed

CITATIONS

6

READS

38

5 AUTHORS, INCLUDING:



Wei Yi

Chinese Academy of Sciences

65 PUBLICATIONS 2,793 CITATIONS

SEE PROFILE



Qifeng Liang

Shaoxing University

27 PUBLICATIONS 169 CITATIONS

SEE PROFILE



Yoshitaka Matsushita

National Institute for Materials Science

160 PUBLICATIONS 2,068 CITATIONS

SEE PROFILE

High-Pressure Synthesis, Crystal Structure, and Properties of $\text{In}_2\text{NiMnO}_6$ with Antiferromagnetic Order and Field-Induced Phase Transition

Wei Yi,^{*,†} Qifeng Liang,[‡] Yoshitaka Matsushita,[§] Masahiko Tanaka,[§] and Alexei A. Belik^{*,†}

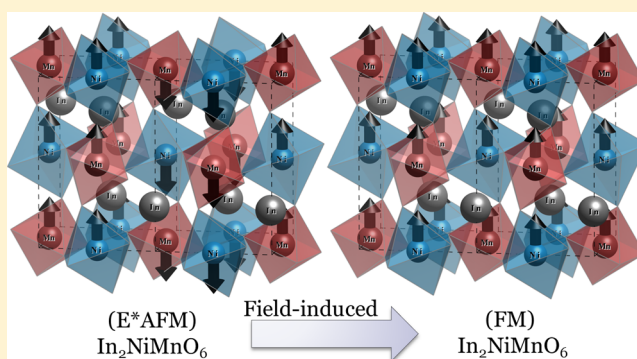
[†]International Center for Materials Nanoarchitectonics (WPI-MANA), National Institute for Materials Science (NIMS), 1-1 Namiki, Tsukuba, Ibaraki 305-0044, Japan

[‡]Department of Physics, University of ShaoXing, Shaoxing 312000, People's Republic of China

[§]Spring-8 Office, National Institute for Materials Science (NIMS), Kohto 1-1-1, Sayo-cho, Hyogo 679-5148, Japan

Supporting Information

ABSTRACT: $\text{In}_2\text{NiMnO}_6$, a new compound extending the family of double rare-earth perovskites R_2NiMnO_6 (R = rare earth, Y) to smaller R ions, was prepared using a high-pressure and high-temperature technique (6 GPa and 1600 K). Its crystal structure was investigated by synchrotron X-ray powder diffraction at room temperature: space group $P2_1/n$ (No. 14, cell choice 2), $Z = 2$, $a = 5.13520(1)$ Å, $b = 5.33728(1)$ Å, $c = 7.54559(4)$ Å, and $\beta = 90.1343(1)^\circ$. A significant degree of ordering of Mn^{4+} and Ni^{2+} ions was observed. The dc and ac magnetization and specific heat measurements showed that $\text{In}_2\text{NiMnO}_6$ is an antiferromagnet with a Néel temperature T_N of 26 K. Its antiferromagnetism puts it apart from other members of the R_2NiMnO_6 family where a ferromagnetic ground state was observed, which is attributed to the superexchange interaction between Mn^{4+} and Ni^{2+} ions according to the Kanamori–Goodenough rules. A field-induced phase transition to a ferromagnetic state was observed from 18 kOe at 5 K, indicating that $\text{In}_2\text{NiMnO}_6$ is close to the antiferromagnetic–ferromagnetic transition boundary. First-principles calculations allowed us to explain its antiferromagnetism and the field-induced phase transition and predict the E^* type antiferromagnetic ground state.



1. INTRODUCTION

In recent years, multiferroic materials, in which ferromagnetic (FM) and ferroelectric (FE) orders coexist, have attracted a great deal of attention in fundamental physics and chemistry^{1–6} because of their great potential for device applications such as nonvolatile memories and sensors.^{4,6} Unfortunately, there exist relatively few magnetoelectric multiferroics in nature and most of them are antiferromagnetic (AFM).^{7–10} For example, BiFeO_3 is a well-known AFM–FE material, with both the Néel temperature $T_N = 650$ K and the ferroelectric Curie temperature $T_E = 1123$ K above room temperature.^{11,12} (Bi,Pb) MO_3 ($\text{M} = \text{Ni, Co, Cr, V}$) were also found to be AFM.^{13–16} This is due to an AFM superexchange interaction between transition-metal (TM) ions via oxygen ions according to the Kanamori–Goodenough (KG) rules.^{17,18} In simple perovskite (ABO_3) materials, the AFM superexchange interaction is induced between the same TM ion orbitals (t_{2g} or e_g) via overlapping with oxygen ion orbitals ($p\pi$ or $p\sigma$) in a B–O–B (almost) linear arrangement. Note that there is one exception: the ferromagnetism of BiMnO_3 is believed to originate from a specific orbital order.¹⁹ Therefore, double perovskite oxides with general formula $\text{A}_2\text{BB}'\text{O}_6$ are needed, where there are two

different 3d TM ions (B and B'), in order to give rise to an intrinsic strong FM interaction. According to the KG rules, ferromagnetism appears if one TM ion with e_g electrons (B) and another without e_g electrons (B') are ordered ($\text{B–O–B}'$) in a rock-salt manner at the B sites of the perovskite structure. This strategy has resulted in FM La_2MMnO_6 ($\text{M} = \text{Co, Ni, Cu}$) materials,^{20–23} multiferroic R_2CoMnO_6 ($\text{R} = \text{Y, Lu}$) materials,²⁴ and the design and realization of the new FM FE material $\text{Bi}_2\text{NiMnO}_6$.^{25–28}

R_2NiMnO_6 (R = rare earth, Y) have attracted much interest and have been studied extensively. The reason is not only because of their ferromagnetism (when Ni^{2+} and Mn^{4+} are ordered) and different magnetic properties depending on the degree of ordering of Ni^{2+} and Mn^{4+} ions^{29–31} but also because of magnetic-field-induced changes in electrical resistivity and dielectric properties.³² Especially, when $\text{R} = \text{La}$, the FM Curie temperature T_C can be 280 K, close to room temperature. A progressive increase of distortions of the perovskite structure

Received: July 24, 2013

Published: December 3, 2013

and a decrease of FM ordering temperature were observed with the decrease of R^{3+} ionic radius from La^{3+} to Lu^{3+} .^{29,31}

In-based and Sc-based perovskites have recently attracted more and more attention in the search for new room-temperature multiferroic materials and exotic physical properties.^{33–41} So far, ScVO_3 ,³⁷ ScCrO_3 ,³⁸ ScRhO_3 ,³⁹ $\text{ScCr}_{1-x}\text{Fe}_x\text{O}_3$,^{38,40} ScMnO_3 ,⁴¹ InCrO_3 ,³⁸ $\text{InCr}_{1-x}\text{Fe}_x\text{O}_3$,³⁸ $(\text{In}_{1-x}\text{Mn}_x)\text{MnO}_3$,³⁴ and InRhO_3 ³⁹ compounds and their solid solutions can be prepared by the high-pressure–high-temperature (HP-HT) method. We thus focused on the In-based double perovskite $\text{In}_2\text{NiMnO}_6$. Several compounds are known in the In–Ni–Mn–O system: InMnO_3 , $(\text{In}_{1-x}\text{Mn}_x)\text{MnO}_3$, and $\text{In}_2\text{Mn}_2\text{O}_7$. Stoichiometric InMnO_3 has so far been obtained only in the hexagonal modification isostructural with $h\text{-RMnO}_3$ ($R = \text{Sc}, \text{Y}, \text{Ho}–\text{Lu}$) even using the HP-HT method.^{33,42} Nonstoichiometric $(\text{In}_{1-x}\text{Mn}_x)\text{MnO}_3$ was stabilized in a monoclinically distorted GdFeO_3 -type perovskite structure (space group $P2_1/n$).³⁴ Manganites with the composition $\text{R}_2\text{Mn}_2\text{O}_7$ ($R = \text{In}, \text{Tl}, \text{Sc}, \text{Y}, \text{Dy}–\text{Lu}$) crystallize in the pyrochlore structure with space group $Fd\bar{3}m$. All $\text{R}_2\text{Mn}_2\text{O}_7$ compounds are FM. In order to stabilize the only Mn^{4+} oxidation state, higher pressure is required for smaller cations ($R = \text{In}, \text{Tl}, \text{Sc}$) in comparison with $R = \text{Dy}–\text{Lu}, \text{Y}$.^{43–45} To the best of our knowledge, there is no information about InNiO_3 or other compounds in the In–Ni–O system.

In the R_2NiMnO_6 family, on further decrease of the R^{3+} ionic radius from Lu^{3+} to In^{3+} , increased structural distortions might lead to interesting physical properties, although the perovskite structure becomes unstable (at ambient pressure). Indeed, the preparation of the “exotic” double perovskite $\text{In}_2\text{NiMnO}_6$ requires HP-HT conditions, because its tolerance factor ($t = 0.774$ with $r_{\text{VI}}(\text{In}^{3+}) = 0.80 \text{ \AA}$ or $t = 0.816$ with $r_{\text{VIII}}(\text{In}^{3+}) = 0.92 \text{ \AA}$) is beyond the stability range of perovskites at ambient pressure.⁴⁶ Here, we report on the synthesis and physical properties of $\text{In}_2\text{NiMnO}_6$.

2. EXPERIMENTAL SECTION

Polycrystalline samples were prepared from stoichiometric mixtures of In_2O_3 (99.99%), NiO (99.9%), and MnO_2 (99.997%) in a molar ratio of 1:1:1. The mixtures were carefully ground using an agate mortar and then sealed in Au capsules. $\text{In}_2\text{NiMnO}_6$ was synthesized by the solid-state reaction method in a belt-type high-pressure apparatus. After a high pressure of 6 GPa and a high temperature of 1600 K were maintained for 2 h, the samples were quenched to room temperature, and then the pressure was slowly released. No noticeable changes in the weight of Au capsules were found after the synthesis, indicating that the target oxygen content in samples did not change during the reaction. The accuracy of the balance used in this work was 0.01 mg. The resultant samples were black dense pellets with a mass of about 0.5 g (for each pellet). The phase purity and oxygen content of MnO_2 were checked and confirmed before its use.

X-ray powder diffraction (XRPD) data for phase analysis were collected at room temperature on a RIGAKU Ultima III diffractometer using $\text{Cu K}\alpha$ radiation. The step-scan measuring method was carried out with a 2θ range of $10–80^\circ$, a step width of 0.02° , and a counting time of 10 s/step. Synchrotron X-ray powder diffraction (SXRPD) data for the structure refinements were collected at room temperature using a large Debye–Scherrer camera at the BL15XU NIMS beamline in SPring-8.⁴⁷ The incident beam using an undulator was monochromated to $\lambda = 0.63043 \text{ \AA}$. The sample was contained in a Lindemann glass capillary tube with an inner diameter of 0.1 mm, and the capillary tube was rotated during measurement. The SXRPD data was collected with 2θ between 1 and 57° and a step interval of 0.003° . The diffraction data were analyzed by the Rietveld method.⁴⁸ The Rietveld refinement was performed using the program RIETAN-FP.⁴⁹ The background was fit with a polynomial function with 12

refined parameters. The occupation factors were fixed at unity for all atoms in the final refinement. Isotropic atomic displacement parameters, B , were assigned to all atoms. For impurities, we refined only scale factors and lattice parameters fixing their structure parameters.

Surface area measurements were carried out using a Hitachi S-4800 field emission scanning electron microscope (FE-SEM) equipped with an energy-dispersive X-ray spectrometer (EDX). EDX analyses were performed with an accelerating voltage of 15 kV. Electron probe microanalysis (EPMA) was performed using a JEOL JXA-8500F instrument. The surface was polished with a fine alumina ($0.3 \mu\text{m}$) coated film before the EPMA measurements, and MnO , NiO , and In_2Se_3 were used as standard samples for Mn, Ni, and In, respectively.

The dc magnetic susceptibilities ($\chi = M/H$) were measured on a SQUID magnetometer (Quantum Design, MPMS) between 2 and 400 K in applied fields of 0.1, 1.0, 10, 20, 30, 40, 50, 60, and 70 kOe under both zero-field-cooled (ZFC) and field-cooled (FC) conditions (FC curves were measured on cooling after ZFC measurements). Isothermal magnetization measurements were performed on the MPMS between -70 and 70 kOe at 5, 50, and 300 K . The ac magnetic susceptibilities at a zero static magnetic field (H_{dc}) were measured on the MPMS from 2 to 70 K at frequencies (f) of 0.5, 2, 7, 25, 110, and 300 Hz and an applied oscillating magnetic field (H_{ac}) of 5 Oe (the maximum H_{ac} value of our instrument). The specific heat, C_p , at different magnetic fields ($H = 0, 10, 20, 30, 40, 50, 60, 70, 80$, and 90 kOe) was recorded between 2 and 300 K (using an N Apiezon grease to make good thermal contacts between a sample and a holder) on a Quantum Design PPMS instrument.

The AFM and FM spin arrangement models were also investigated by density functional theory (DFT) calculations using the Vienna ab initio simulation package (VASP)⁵⁰ with the projected augmented plane-wave (PAW) method and the generalized gradient approximation (GGA) by Perdew, Burke, and Ernzerhof for the exchange correlation function.⁵¹ An energy cutoff of 400 eV was employed, and a $6 \times 6 \times 6$ momentum mesh was used to ensure the convergence of calculations.

3. RESULTS AND DISCUSSION

The SXRPD pattern at room temperature showed that the sample contained small amounts of impurities: $\text{In}_2\text{Mn}_2\text{O}_7$, NiO , and rhombohedral In_2O_3 . The weight fraction of the main phase was estimated to be more than 93% after the Rietveld analysis. All of our attempts to eliminate impurities by varying synthesis conditions and starting stoichiometry failed. All reflections of the main phase were indexed using TREOR⁵² in a monoclinic system. The observed reflection conditions of $k + l = 2n$ for $h0l$, $h00$, and $00l$ and $k = 2n$ for $0k0$ afforded the possible centrosymmetric space group $P2_1/n$ (No. 14, cell choice 2) similar to the case for the double rare-earth perovskites R_2NiMnO_6 ($R = \text{rare earth}, \text{Y}$). Therefore, the structure parameters of $\text{Tb}_2\text{NiMnO}_6$ were used as the initial values for the refinement of $\text{In}_2\text{NiMnO}_6$.³¹

The refined structural parameters, R values, selected bond lengths, and bond-valence sums (BVS)⁵³ of $\text{In}_2\text{NiMnO}_6$ are given in Tables 1 and 2. Experimental, calculated, and difference SXRPD profiles are shown in Figure 1. The crystal structure of $\text{In}_2\text{NiMnO}_6$ is shown in the inset of Figure 1. The BVS values of $+2.003(9)$ for the Ni site (2d site) and $+4.048(8)$ for the Mn site (2c site) support the proposed ionic distribution and oxidation states. The refinement of occupation factors (g) of the Ni and Mn sites resulted in $g(\text{Ni}) = 1.005(2)$ and $g(\text{Mn}) = 0.984(2)$ with $g = 1$ for all other sites and fixed $B(\text{Ni})$ and $B(\text{Mn})$ (and with the refinement of all other structural parameters (given in Table 1), profile parameters, zero-shift parameters, and background parameters).

Table 1. Crystallographic Parameters of $\text{In}_2\text{NiMnO}_6$ at Room Temperature^a

site	Wyckoff position	x	y	z	B (Å ²)
Mn	2c	0.5	0.0	0.5	0.28(2)
Ni	2d	0.5	0.0	0.0	0.26(1)
In	4e	0.98048(6)	0.06111(5)	0.25257(6)	0.402(6)
O1	4e	0.3804(5)	0.9363(5)	0.2621(4)	0.49(5)
O2	4e	0.1992(6)	0.1844(6)	0.5626(4)	0.44(6)
O3	4e	0.6784(5)	0.2914(6)	0.4313(4)	0.34(6)

^aParameters: wavelength $\lambda = 0.63043$ Å, space group $P2_1/n$ (No. 14 cell choice 2), $Z = 2$, $a = 5.13520(1)$ Å, $b = 5.33728(1)$ Å, $c = 7.54559(4)$ Å, $\beta = 90.1343(1)^\circ$, $\rho_{\text{calc}} = 7.054$ g/cm³, $V = 206.809(5)$ Å³. Occupation factors of all of the sites are unity. R values (%): $R_{\text{wp}} = 6.66$, $R_p = 4.58$, $R_B = 3.49$, and $R_F = 2.28$. The weight fractions of In_2O_3 , NiO , and $\text{In}_2\text{Mn}_2\text{O}_7$ are 4.6%, 0.5%, and 1.1%, respectively.

Table 2. Selected Bond Lengths (Å), Bond-Valence Sums (BVS), and Bond Angles (deg) for $\text{In}_2\text{NiMnO}_6$ ^a

Mn–O1 (×2)	1.926(3)	In–O2	2.126(3)
Mn–O2 (×2)	1.893(3)	In–O1	2.129(3)
Mn–O3 (×2)	1.879(3)	In–O3	2.158(3)
BVS (Mn ⁴⁺)	4.048(8)	In–O1	2.160(3)
		In–O3	2.397(3)
Ni–O1 (×2)	2.100(3)	In–O2	2.445(3)
Ni–O2 (×2)	2.057(3)	In–O2	2.675(3)
Ni–O3 (×2)	2.057(3)	In–O3	2.746(3)
BVS (Ni ²⁺)	2.003(9)	BVS (In ³⁺)	2.804(5)
Mn–O3–Ni	140.4(2)	Mn–O2–Ni	141.8(2)
Mn–O1–Ni	139.1(1)		

^aBVS = $\sum_{i=1}^N \nu_i$, $\nu_i = \exp[(R_0 - l_i)/B]$, N is the coordination number, $B = 0.37$, $R_0(\text{Mn}^{4+}) = 1.753$, $R_0(\text{Ni}^{2+}) = 1.654$, and $R_0(\text{In}^{3+}) = 1.902$.⁵³

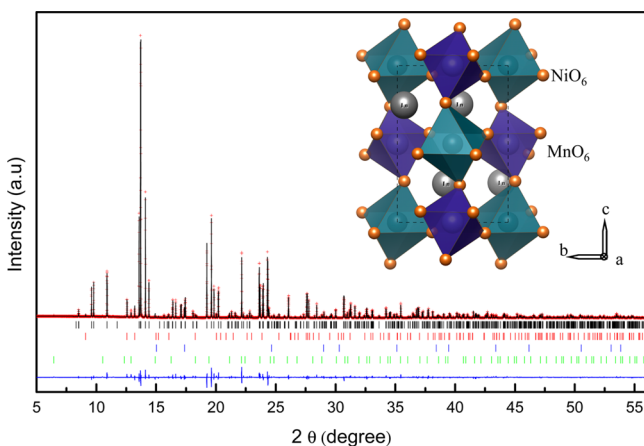


Figure 1. Fragment of the observed (+), calculated (—), and difference synchrotron XRPD patterns of $\text{In}_2\text{NiMnO}_6$. Bragg reflections are indicated by tick marks for $\text{In}_2\text{NiMnO}_6$ (top). The lower tick marks are given for the impurity phases In_2O_3 (second from top), NiO (third from top), and $\text{In}_2\text{Mn}_2\text{O}_7$ (bottom). The inset shows a fragment of the crystal structure of $\text{In}_2\text{NiMnO}_6$ along the a axis. NiO_6 and MnO_6 octahedra are shown.

We note that the structural analysis with a random distribution of Ni^{2+} and Mn^{4+} ions between the 2d and 2c sites gave larger R values ($R_{\text{wp}} = 6.93\%$, $R_p = 4.78\%$, $R_B = 3.55\%$, and $R_F = 2.30\%$), but most importantly the subsequent refinement of the occupation factors for a virtual atom (VA), $\text{VA} = 0.5\text{Mn}^{4+} + 0.5\text{Ni}^{2+}$, resulted in $g = 0.900(3)$ for the 2c site

and $g = 1.081(3)$ for the 2d site. These facts and the monoclinic structure of $\text{In}_2\text{NiMnO}_6$ suggested that there was a significant degree of ordering of Ni^{2+} and Mn^{4+} ions. For the precise determination of the degree of Ni^{2+} and Mn^{4+} ordering, neutron diffraction data are needed. We note that indium atoms strongly adsorb neutrons; therefore, it is challenging to measure good neutron diffraction data.

The occupation factors for oxygen sites were refined to be $g(\text{O1}) = 1.026(4)$, $g(\text{O2}) = 1.002(6)$, and $g(\text{O3}) = 1.053(6)$ with fixed $g = 1$ for other sites. The occupation factor of the In site was refined to be $g(\text{In}) = 1.000(1)$ with fixed $g = 1$ for other sites. These results strongly suggested that all of the cation and oxygen sites in $\text{In}_2\text{NiMnO}_6$ are fully occupied ($g = 1$). This was in agreement with the result of the EPMA analysis, which gave $\text{Ni}:\text{Mn} = 1.00(3):1.00$, and the EDX analysis, which gave $\text{In}:\text{Ni}:\text{Mn} = 2.09(18):1.05(9):1.00$ (see the Supporting Information). Note that the In content by EPMA was not reliable, probably because of the specific standard material.

The dc magnetic susceptibility ZFC curves of $\text{In}_2\text{NiMnO}_6$ between 2 and 200 K at different magnetic fields from 0.1 to 70 kOe are shown in Figure 2. There was almost no difference between the ZFC and FC curves at a given magnetic field, except for the curves at 0.1 kOe (see the Supporting Information). At small magnetic fields, there were noticeable FM anomalies at around 130 K and a difference between the ZFC and FC curves (at 0.1 kOe) at lower temperature originating from the FM impurity $\text{In}_2\text{Mn}_2\text{O}_7$.^{44,45} However, the contribution from $\text{In}_2\text{Mn}_2\text{O}_7$ was completely suppressed at larger magnetic fields. In the range 0.1–10 kOe, clear AFM-like sharp peaks were observed on both ZFC and FC curves, and the T_N value was almost independent of the field. From 20 kOe, the peak positions started to move to lower temperatures, and the peaks became much broader. At magnetic fields above 50 kOe, almost no peak was observed, and magnetic susceptibilities were typical for ferromagnets (if measured at large magnetic fields).^{29,31,45,54} Therefore, dc magnetic susceptibility measurements showed that there are some changes in the behavior (a field-induced transition) between 10 and 20 kOe.

The magnetic susceptibility curves at 10–70 kOe were fit between 200 and 400 K with the Curie–Weiss equation

$$\chi^{-1}(T) = 3k_B(T - \Theta)/(\mu_{\text{eff}}^2 N_A) \quad (1)$$

where μ_{eff} is the effective magnetic moment, N_A is Avogadro's number, k_B is Boltzmann's constant, and Θ is the Curie–Weiss temperature (see the Supporting Information). At 70 kOe, the fitting parameters $\mu_{\text{eff}} = 4.891(2)\mu_B$ and $\Theta = +58.3(2)$ K were obtained as shown in the inset of Figure 2. The positive Curie–Weiss temperature of 58.3(2) K indicates that FM interactions are dominant. It should be noted that a positive Curie–Weiss temperature was also observed in AFM LaMnO_3 because of the dominant FM interactions in layers.⁵⁵ The effective magnetic moment is in good agreement with the calculated value of $4.796\mu_B/\text{fu}$, expected for Mn^{4+} (d^3 : $t_{2g}^3 e_g^0$) and Ni^{2+} (d^8 : $t_{2g}^6 e_g^2$). The ac susceptibility χ' vs T and χ'' vs T curves obtained at different frequencies (f) are plotted in Figure 3. The χ' vs T curves show frequency-independent peaks at about 26 K, and no anomalies were observed on the χ'' vs T curves, indicating that a transition to a long-range AFM state occurs.

The isothermal magnetization (M vs H) curves of $\text{In}_2\text{NiMnO}_6$ at 5, 50, and 300 K are plotted in Figure 4. An anomaly near the origin at 5 and 50 K originated from the

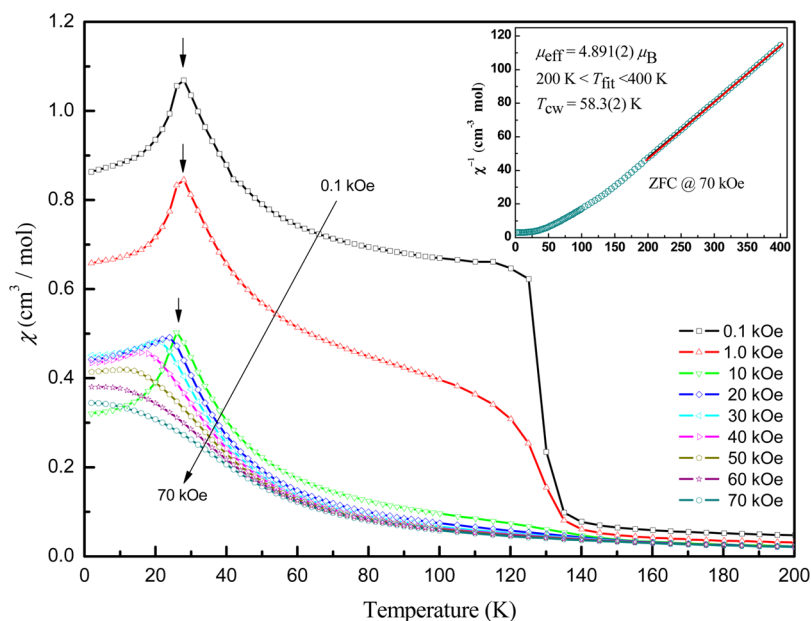


Figure 2. ZFC dc magnetic susceptibility ($\chi = M/H$) curves (χ vs T) of $\text{In}_2\text{NiMnO}_6$ measured at different external static magnetic fields. The inset shows the inverse ZFC magnetic susceptibility curve measured at 70 kOe. The red solid line shows fitting result at temperature range of 200 to 400 K with eq 1.

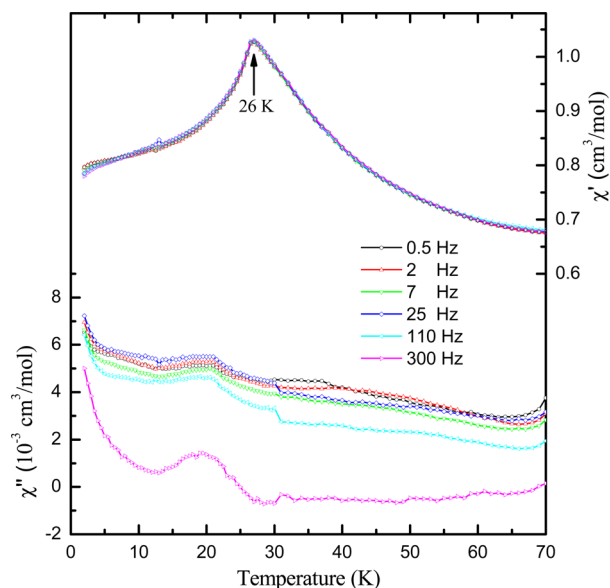


Figure 3. Real (top) and imaginary (bottom) parts of the ac susceptibility vs temperature (χ' vs T and χ'' vs T) at different frequencies (f) in an applied oscillating magnetic field (H_{ac}) of 5 Oe. Measurements were performed in the temperature range 2–70 K and zero static magnetic field ($H_{dc} = 0$ Oe).

$\text{In}_2\text{Mn}_2\text{O}_7$ impurity with soft FM behavior.^{44,45} The M vs H curves at 5 K clearly showed that $\text{In}_2\text{NiMnO}_6$ behaves as a fully compensated antiferromagnet at magnetic fields below about 18 kOe, confirming the results of the temperature-dependent measurements (Figure 2). Above 18 kOe, a field-induced transition was observed with sharper increase of magnetization, again in agreement with the temperature-dependent measurements. The magnetization of $\text{In}_2\text{NiMnO}_6$ reached about $4.3\mu_B/\text{fu}$ at 70 kOe and 5 K, approaching the full magnetization value of $5\mu_B/\text{fu}$.

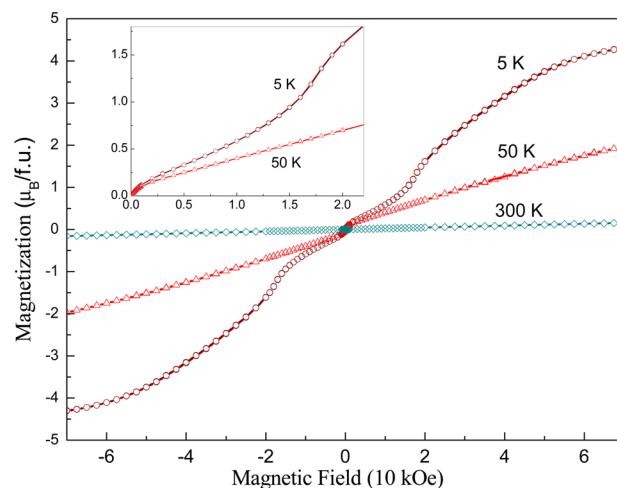


Figure 4. Isothermal magnetization (M vs H) curves of $\text{In}_2\text{NiMnO}_6$ at 5 K (circles), 50 K (triangles), and 300 K (diamonds) between -70 and 70 kOe. The inset presents the M vs H curves at 5 K (circles) and 50 K (triangles) in the magnetic field range 0–20 kOe.

Figure 5 shows the specific heat of $\text{InNi}_{0.5}\text{Mn}_{0.5}\text{O}_3$ plotted as C_p/T versus temperature (C_p/T vs T) in the temperature range 2–100 K at magnetic fields from 0 to 90 kOe. The specific heat showed one peak at 26 K at 0 Oe, which was consistent with the peaks on the χ vs T curves and χ' vs T curves. The peaks gradually shifted to lower temperatures (as expected for antiferromagnets) and smeared with an increase in the magnetic field. However, at the same time, a magnetic contribution increased at high temperatures above 30 K up to 100 K. This behavior is quite typical for ferromagnets: for example, BiMnO_3 ,⁵⁴ where a magnetic field (of 90 kOe) completely removed a specific heat anomaly at $T_C = 102$ K and introduced a magnetic contribution to the specific heat up to 170 K. The magnetic entropy of $\text{InNi}_{0.5}\text{Mn}_{0.5}\text{O}_3$ at 0 Oe was estimated to be $8.65 \text{ J K}^{-1} \text{ mol}^{-1}$ (see the Supporting

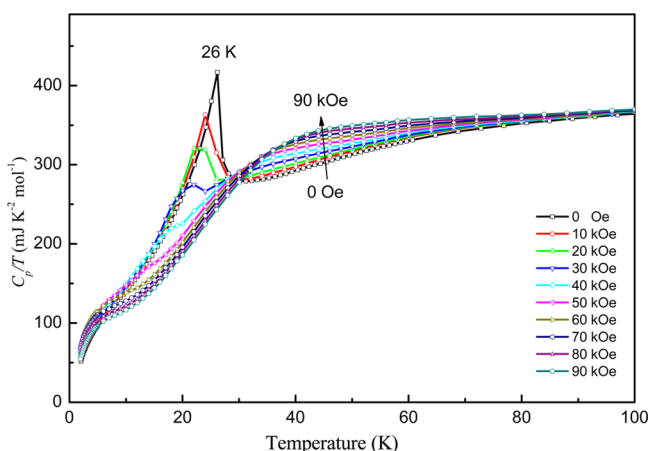


Figure 5. C_p/T vs T curves between 2 and 100 K for $\text{InNi}_{0.5}\text{Mn}_{0.5}\text{O}_3$ (the molecular weight is calculated for the ABO_3 composition) at different magnetic fields (from 0 to 90 kOe with a step of 10 kOe).

Information), close to the magnetic entropy of InCrO_3 ($9.04 \text{ J K}^{-1} \text{ mol}^{-1}$).³⁸

In Figure 6, we compare the lattice parameters, unit cell volume, Ni–O–Mn bond angles, and magnetic ordering temperature of $\text{In}_2\text{NiMnO}_6$ with those of the R_2NiMnO_6 family.^{29,31} Monotonic changes as a function of the R^{3+} ionic radius were observed in the unit cell volumes, Ni–O–Mn bond angles, and magnetic ordering temperatures. However, the lattice parameters of $\text{In}_2\text{NiMnO}_6$ exhibit nonmonotonic changes. Similar features in the lattice parameters were found in RRhO_3 and RCrO_3 ($\text{R} = \text{Sc}, \text{In}, \text{Y}, \text{La-Lu}$) and attributed to significant hybridization of In–O bonds resulting in more covalent bonds in comparison with R-O ($\text{R} = \text{Sc}, \text{Y}, \text{La-Lu}$)

bonds.³⁹ In comparison with the other members of R_2NiMnO_6 , the Ni–O–Mn bond angles in $\text{In}_2\text{NiMnO}_6$ (139.1 , 141.8 , and 140.4°) were the smallest and deviated the most from 180° .

The empirical KG rules predicted the right FM ground states for all of the previously known members in the R_2NiMnO_6 family with a scenario of superexchange interaction between the half-filled e_g orbital of Ni^{2+} and the vacant e_g orbital of Mn^{4+} through the p orbital of O^{2-} . However, due to the structural distortion of the perovskites, the Ni–O–Mn angles deviated from 180° with a decrease in the radius of R^{3+} cations. Smaller Ni–O–Mn angles give rise to smaller hopping strengths between the cations and O anions and, therefore, effectively reduce the FM coupling between the cations. First, this effect results in a monotonic decrease of the FM ordering temperature T_C with a decrease in the Ni–O–Mn bond angles (Figure 6d).^{29,31} Second, the effect of decreasing the Ni–O–Mn bond angles could result in the stabilization of an AFM ground state. Indeed, it was theoretically predicted by Kumar et al.⁵⁶ that the magnetic ground state should change from FM for $\text{La}_2\text{NiMnO}_6$ to AFM for Y_2NiMnO_6 due to a decrease of the rare-earth ionic size from La^{3+} (1.160 \AA) to Y^{3+} (1.019 \AA), in disagreement with the experimental observations that Y_2NiMnO_6 is a FM insulator with $T_C = 79 \text{ K}$.³¹ An AFM ground state is realized in $\text{In}_2\text{NiMnO}_6$ with smaller In^{3+} ions (0.92 \AA) at the A site in comparison with Y^{3+} (1.019 \AA). To understand the possible reasons, we performed density functional calculations as described below.

The DFT total energies of the different magnetic structures were investigated when GGA + U (U is the effective local two-electron repulsion term) was applied with the value of U in the range 0–5 eV. When $U < 2.0 \text{ eV}$, the first-principles calculation results showed that many AFM spin arrangements are energetically more stable than the FM spin arrangement.

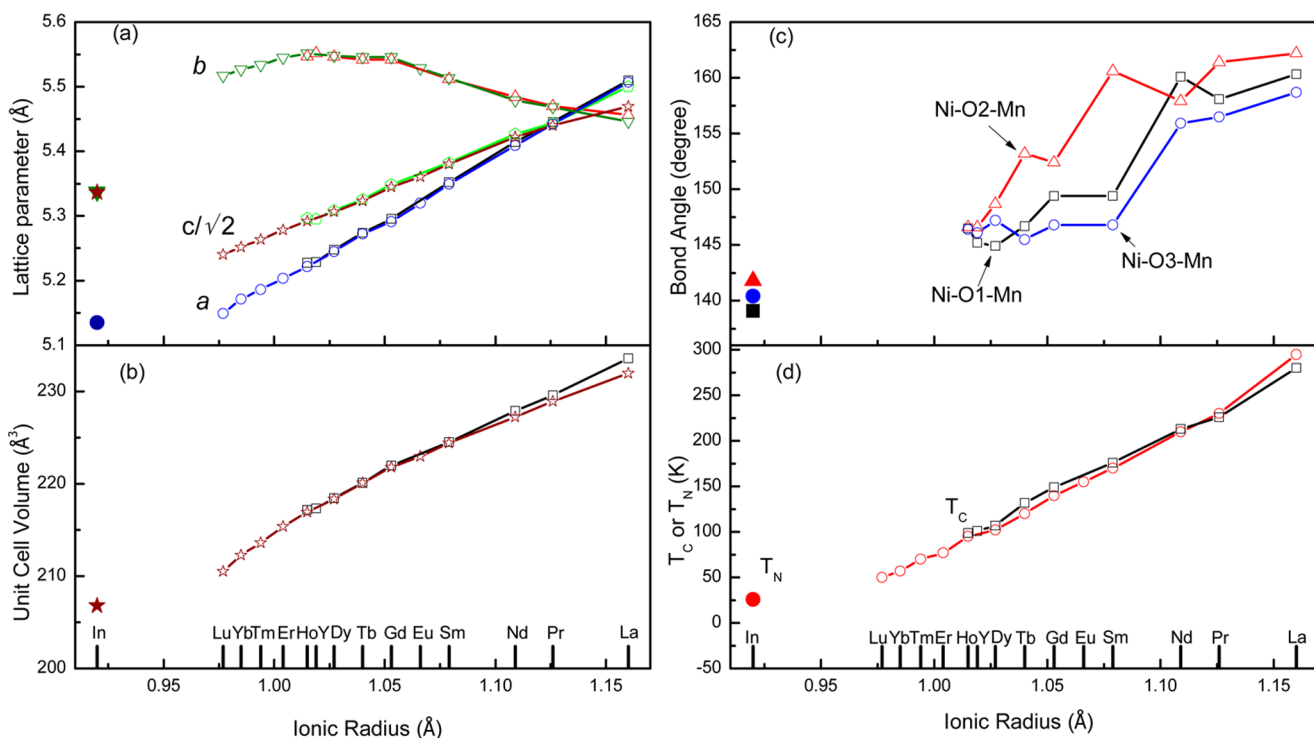


Figure 6. (a) Lattice parameters, (b) unit cell volumes, (c) Ni–O–Mn bond angles, and (d) magnetic ordering temperatures (T_N for AFM and T_C for FM) as a function of the R^{3+} ionic radius (in the 8-fold coordination) in R_2NiMnO_6 ($\text{R} = \text{La-Lu}, \text{Y},^{29,31} \text{In}$). The lines are drawn as guides for the eye.

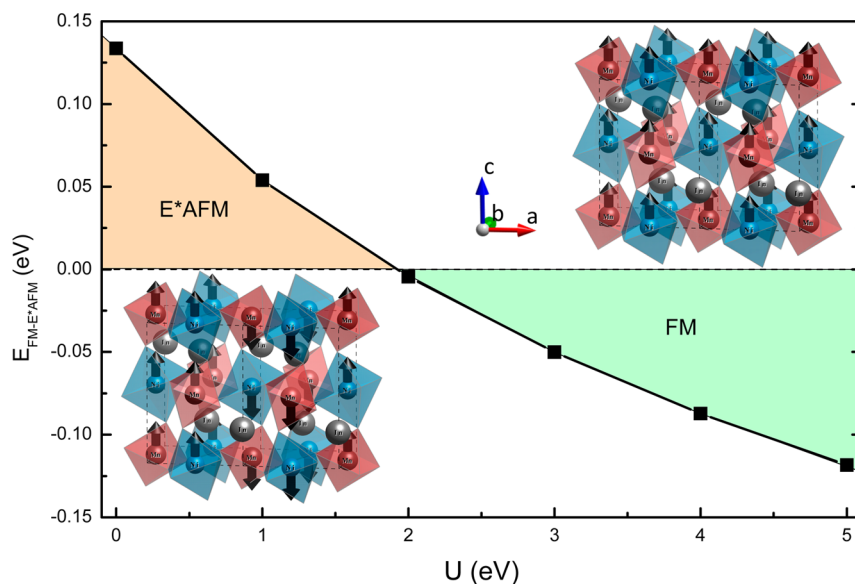


Figure 7. Total energy difference per two unit cells (along the *a* axis) between an E*-type antiferromagnetic arrangement and ferromagnetic arrangement ($E_{\text{FM-E*AFM}}$) as a function of U (black solid squares). The lines are drawn as guides for the eye. The insets show the E*-type antiferromagnetic (lower left)⁵⁶ and ferromagnetic (upper right) arrangements in the $2 \times 1 \times 1$ unit cell. Arrows show the direction of magnetic spins.

When the value of U is higher than 2.0 eV, the FM spin configuration is energetically more stable. Among possible AFM spin arrangements in a doubled unit cell at small U region, we found that an E*-type AFM (E*AFM) spin arrangement (Figure 7)⁵⁶ has the lowest total energy, which could be the correct ground state of $\text{In}_2\text{NiMnO}_6$. The total energy difference between E*AFM and FM ($E_{\text{FM-E*AFM}}$) as a function of U from 0 to 5 eV is shown in Figure 7. In this E*AFM spin configuration, spins couple ferromagnetically in the *bc* plane, while in the *a* axis they are arranged in an up–up–down–down zigzag configuration. With this layered AFM spin arrangement, we can explain the experimental fact that $\text{In}_2\text{NiMnO}_6$ has an AFM ground state but has strong FM coupling, as evidenced by the positive Curie–Weiss temperature. It must be noted that the energy difference $E_{\text{FM-E*AFM}}$ was very small when the U value was equal to 2 eV. Therefore, an external magnetic field could overcome a small energy difference and induce an AFM to FM transition, as was observed experimentally from 18 kOe at 5 K in $\text{In}_2\text{NiMnO}_6$. To be in agreement with the experimental observations for $\text{In}_2\text{NiMnO}_6$ the U values should not exceed 2 eV. Therefore, we suggest that an effective U value of 2 eV, although smaller than typical values for 3d transition-metal oxides (about 3 eV in $\text{La}_2\text{NiMnO}_6$;⁵⁷ $U_{\text{Mn}} = 3.5$ eV and $U_{\text{Ni}} = 4.0$ eV in $\text{Bi}_2\text{NiMnO}_6$ ⁵⁸), should be adopted for the R_2NiMnO_6 family. Using the same set of U parameters on Ni and Mn d electrons, we obtained the FM ground state for Y_2NiMnO_6 and $\text{La}_2\text{NiMnO}_6$. Previous DFT calculations without U correction⁵⁶ produced an AFM ground state, which obviously disagrees with the experimental FM ground state.^{29,31}

The magnetic ground state of $\text{In}_2\text{NiMnO}_6$ can be probed directly by neutron diffraction. However, we have some indirect evidence for the proposed E*AFM ground state. First, the magnetic unit cell is doubled in the E*AFM structure in comparison with the crystallographic unit cell. Therefore, the E*AFM structure cannot support weak ferromagnetism (or spin canting) by the symmetry;⁵⁹ we indeed observed that $\text{In}_2\text{NiMnO}_6$ is a fully compensated antiferromagnet (below 18

kOe) similar to RMnO_3 ($R = \text{Ho–Lu}$), which have a close collinear E-type AFM structure.^{60,61} Second, the E*AFM structure breaks the inversion symmetry⁵⁶ and results in electrical polarization;^{24,60,62} we indeed observed sharp dielectric anomalies at T_N of $\text{In}_2\text{NiMnO}_6$. Detailed dielectric studies of $\text{In}_2\text{NiMnO}_6$ will be reported elsewhere.

4. CONCLUSION

A new compound, $\text{In}_2\text{NiMnO}_6$, extending the family of double perovskites R_2NiMnO_6 was prepared using a HP-HT technique (at 6 GPa and 1600 K). Its crystal structure was investigated by synchrotron X-ray powder diffraction, and it crystallizes in the B-site-ordered structure with space group $P2_1/n$. A significant degree of ordering of Mn^{4+} and Ni^{2+} ions was found. Magnetic properties were studied using dc and ac magnetization and specific heat measurements. $\text{In}_2\text{NiMnO}_6$ is an antiferromagnet with a Néel temperature of 26 K, in contrast with other members of the R_2NiMnO_6 family, which are ferromagnetic. A field-induced phase transition to a ferromagnetic state was observed from 18 kOe at 5 K, indicating that $\text{In}_2\text{NiMnO}_6$ is close to the antiferromagnetic–ferromagnetic transition boundary. First-principles calculations allowed us to explain its antiferromagnetism and the field-induced phase transition. In our future work, $\text{Sc}_2\text{NiMnO}_6$ with even smaller Sc^{3+} cations at the A site will be investigated and compared with $\text{In}_2\text{NiMnO}_6$.

■ ASSOCIATED CONTENT

Supporting Information

Tables and figures giving EDX and EPMA analyses of $\text{In}_2\text{NiMnO}_6$, results of Curie–Weiss fits of magnetic susceptibility curves (200–400 K) at different magnetic fields, an SEM image of the $\text{In}_2\text{NiMnO}_6$ surface, ZFC and FC χ vs T curves, ZFC χ^{-1} vs T curve, and ZFC $d(\chi T)/dT$ vs T curves at different magnetic fields, and calculated total energy ΔE per two unit cells of different magnetic configurations relative to the FM configuration of $\text{In}_2\text{NiMnO}_6$. This material is available free of charge via the Internet at <http://pubs.acs.org>.

AUTHOR INFORMATION

Corresponding Authors

*E-mail for W.Y.: YI.Wei@nims.go.jp.

*E-mail for A.A.B.: Alexei.Belik@nims.go.jp.

Notes

The authors declare no competing financial interest.

ACKNOWLEDGMENTS

This work was supported by World Premier International Research Center Initiative (WPI Initiative, MEXT, Japan), the Japan Society for the Promotion of Science (JSPS) through its "Funding Program for World-Leading Innovative R&D on Science and Technology (FIRST Program)", and Grants-in-Aid for Scientific Research (22246083 and 21540330) from JSPS of Japan. The synchrotron radiation experiments were performed at the SPring-8 with the approval of the Japan Synchrotron Radiation Research Institute (Proposal Numbers 2009B4505, 2011B4512, and 2011B4514). Q.L. was also supported by the NSFC under grant no. 10904092. We thank Mr. K. Kosuda of NIMS for the EPMA measurements, Mr. K. Iiyama of NIMS for help with the EDX measurements, and Prof. K. Asai of the University of Electro-Communications (Tokyo) for numerical data from ref 29.

REFERENCES

- Eerenstein, W.; Mathur, N. D.; Scott, J. F. *Nature (London)* **2006**, *442*, 759.
- Ramesh, R. *Nature (London)* **2009**, *461*, 1218.
- Spaldin, N. A.; Cheong, S.-W.; Ramesh, R. *Phys. Today* **2010**, *63*, 38.
- Ramesh, R.; Spaldin, N. A. *Nat. Mater.* **2007**, *6*, 21.
- Lottermoser, T.; Lonkai, T.; Amann, U.; Hohlwein, D.; Ihringer, J.; Fiebig, M. *Nature (London)* **2004**, *430*, 541.
- Fiebig, M.; Spaldin, N. A. *Eur. Phys. J. B* **2009**, *71*, 293.
- Hill, N. A. *J. Phys. Chem. B* **2000**, *104*, 6694.
- Hill, N. A.; Filippetti, A. *J. Magn. Magn. Mater.* **2002**, *242–245*, 976.
- Seshadri, R.; Hill, N. A. *Chem. Mater.* **2001**, *13*, 2892.
- Ederer, C.; Spaldin, N. A. *Curr. Opin. Solid State Mater. Sci.* **2005**, *9*, 128.
- Smolenskii, G. A.; Chupis, I. E. *Sov. Phys. Usp.* **1982**, *25*, 475.
- Catalan, G.; Scott, J. F. *Adv. Mater.* **2009**, *21*, 2463.
- Belik, A. A. *J. Solid State Chem.* **2012**, *195*, 32.
- Belik, A. A.; Iikubo, S.; Kodama, K.; Igawa, N.; Shamoto, S.; Niitaka, S.; Azuma, M.; Shimakawa, Y.; Takano, M.; Izumi, F.; Takayama-Muromachi, E. *Chem. Mater.* **2006**, *18*, 798.
- Ishiwata, S.; Azuma, M.; Takano, M.; Nishibori, E.; Takata, M.; Sakata, M.; Kato, K. *J. Mater. Chem.* **2002**, *12*, 3733.
- Belik, A. A.; Azuma, M.; Saito, T.; Shimakawa, Y.; Takano, M. *Chem. Mater.* **2005**, *17*, 269.
- (a) Goodenough, J. B. *Phys. Rev.* **1955**, *100*, 564. (b) Goodenough, J. B. *Magnetism and the Chemical Bond*; Interscience: New York, 1963.
- Kanamori, J. *J. Phys. Chem. Solids* **1959**, *10*, 87.
- (a) Moreira dos Santos, A.; Cheetham, A. K.; Atou, T.; Syono, Y.; Yamaguchi, Y.; Ohoyama, K.; Chiba, H.; Rao, C. N. R. *Phys. Rev. B* **2002**, *66*, 064425. (b) Gonchar, L. E.; Nikiforov, A. E. *Phys. Rev. B* **2013**, *88*, 094401.
- Sánchez-Benítez, J.; Martínez-Lope, M. J.; Alonso, J. A.; García-Muñoz, J. L. *J. Phys.: Condens. Matter* **2011**, *23*, 226001.
- (a) Dass, R. I.; Yan, J.-Q.; Goodenough, J. B. *Phys. Rev. B* **2003**, *68*, 064415. (b) Dass, R. I.; Goodenough, J. B. *Phys. Rev. B* **2003**, *67*, 014401.
- Blasse, G. *J. Phys. Chem. Solids* **1965**, *26*, 1969.
- Anderson, M. T.; Greenwood, K. B.; Taylor, G. A.; Poeppelmeier, K. R. *Prog. Solid State Chem.* **1993**, *22*, 197.
- (a) Yáñez-Vilar, S.; Mun, E. D.; Zapf, V. S.; Ueland, B. G.; Gardner, J. S.; Thompson, J. D.; Singleton, J.; Sánchez-Andújar, M.; Mira, J.; Biskup, N.; Señaris-Rodríguez, M. A.; Batista, C. D. *Phys. Rev. B* **2011**, *84*, 134427. (b) Sharma, G.; Saha, J.; Kaushik, S. D.; Siruguri, V.; Patnaik, S. *Appl. Phys. Lett.* **2013**, *103*, 012903.
- Azuma, M.; Takata, K.; Saito, T.; Ishiwata, S.; Shimakawa, Y.; Takano, M. *J. Am. Chem. Soc.* **2005**, *127*, 8889.
- Shimakawa, Y.; Azuma, M.; Ichikawa, N. *Materials* **2011**, *4*, 153.
- Sakai, M.; Masuno, A.; Kan, D.; Hashisaka, M.; Takata, K.; Azuma, M.; Takano, M.; Shimakawa, Y. *Appl. Phys. Lett.* **2007**, *90*, 072903.
- Zhao, H.; Chen, X. *AIP Adv.* **2012**, *2*, 042143.
- Asai, K.; Fujiyoshi, K.; Nishimori, N.; Satoh, Y.; Kobayashi, Y.; Mizoguchi, M. *J. Phys. Soc. Jpn.* **1998**, *67*, 4218.
- Asai, K.; Kobayashi, N.; Bairo, T.; Kaneko, N.; Kobayashi, Y.; Suzuki, M.; Satoh, Y.; Mizoguchi, M. *J. Phys. Soc. Jpn.* **2005**, *74*, 1289.
- Booth, R. J.; Fillman, R.; Whitaker, H.; Nag, A.; Tiwari, R. M.; Ramanujachary, K. V.; Gopalakrishnan, J.; Lofland, S. E. *Mater. Res. Bull.* **2009**, *44*, 1559.
- Rogado, N. S.; Li, J.; Sleight, A. W.; Subramanian, M. A. *Adv. Mater.* **2005**, *17*, 2225.
- Belik, A. A.; Furubayashi, T.; Matsushita, Y.; Tanaka, M.; Hishita, S.; Takayama-Muromachi, E. *Angew. Chem., Int. Ed.* **2009**, *48*, 6117.
- Belik, A. A.; Furubayashi, T.; Matsushita, Y.; Tanaka, M.; Takayama-Muromachi, E. *Angew. Chem., Int. Ed.* **2010**, *49*, 7723.
- Belik, A. A.; Kamba, S.; Savinov, M.; Nuzhnyy, D.; Tachibana, M.; Takayama-Muromachi, E.; Goian, V. *Phys. Rev. B* **2009**, *79*, 054411.
- Fabre, X.; Mirebeau, I.; Petit, S.; Bonville, P.; Belik, A. A. *Phys. Rev. B* **2011**, *84*, 054455.
- Castillo-Martinez, E.; Bieringer, M.; Shafi, S. P.; Cranswick, L. M. D.; Alario-Franco, M. A. *J. Am. Chem. Soc.* **2011**, *133*, 8552.
- Belik, A. A.; Matsushita, Y.; Tanaka, M.; Takayama-Muromachi, E. *Chem. Mater.* **2012**, *24*, 2197.
- Belik, A. A.; Matsushita, Y.; Tanaka, M.; Takayama-Muromachi, E. *Inorg. Chem.* **2013**, *52*, 12005.
- Li, M. R.; Adem, U.; McMitchell, S. R. C.; Xu, Z. L.; Thomas, C. I.; Warren, J. E.; Giap, D. V.; Niu, H. J.; Wan, X. M.; Palgrave, R. G.; Schiffmann, F.; Cora, F.; Slater, B.; Burnett, T. L.; Cain, M. G.; Abakumov, A. M.; van Tendeloo, G.; Thomas, M. F.; Rosseinsky, M. J.; Claridge, J. B. *J. Am. Chem. Soc.* **2012**, *134*, 3737.
- Chen, H.; Yu, T.; Gao, P.; Bai, J.; Tao, J.; Tyson, T. A.; Wang, L.; Lalancette, R. *Inorg. Chem.* **2013**, *52*, 9692.
- Greedan, J. E.; Bieringer, M.; Britten, J. F.; Giaquinta, D. M.; zur Loye, H. C. *J. Solid State Chem.* **1995**, *116*, 118.
- Greedan, J. E.; Raju, N. P.; Subramanian, M. A. *Solid State Commun.* **1996**, *99*, 399.
- Raju, N. P.; Greedan, J. E.; Subramanian, M. A. *Phys. Rev. B* **1994**, *49*, 1086.
- Shimakawa, Y.; Kubo, Y.; Hamada, N.; Jorgensen, J. D.; Hu, Z.; Short, S.; Nohara, M.; Takagi, H. *Phys. Rev. B* **1999**, *59*, 1249.
- Eitel, R. E.; Randall, C. A.; Shrout, T. R.; Rehrig, P. W.; Hackenberger, W.; Park, S. E. *Jpn. J. Appl. Phys., Part 1* **2001**, *40*, 5999.
- Tanaka, M.; Katsuya, Y.; Yamamoto, A. *Rev. Sci. Instrum.* **2008**, *79*, 075106.
- Rietveld, H. M. *J. Appl. Crystallogr.* **1969**, *2*, 65.
- Izumi, F.; Momma, K. *Solid State Phenom.* **2007**, *130*, 15.
- Kresse, G.; Furthmüller, J. *Phys. Rev. B* **1996**, *54*, 11169.
- Perdew, J. P.; Burke, K.; Ernzerhof, M. *Phys. Rev. Lett.* **1996**, *77*, 3865.
- Werner, P. E.; Eriksson, L.; Westdahl, M. *J. Appl. Crystallogr.* **1985**, *18*, 367.
- Brese, N. E.; O'Keeffe, M. *Acta Crystallogr., Sect. B* **1991**, *47*, 192.
- Belik, A. A.; Takayama-Muromachi, E. *Inorg. Chem.* **2006**, *45*, 10224.
- (a) Zhou, J. S.; Goodenough, J. B. *Phys. Rev. B* **1999**, *60*, 15002(R). (b) Ritter, C.; Ibarra, M. R.; De Teresa, J. M.; Algarabel, P.

A.; Marguina, C.; Blasco, J.; Garcia, J.; Oseroff, S.; Cheong, S. W. *Phys. Rev. B* **1997**, *56*, 8902.

(56) Kumar, S.; Giovannetti, G.; van den Brink, J.; Picozzi, S. *Phys. Rev. B* **2010**, *82*, 134429.

(57) Das, H.; Waghmare, U. V.; Saha-Dasgupta, T.; Sarma, D. D. *Phys. Rev. Lett.* **2008**, *100*, 186402.

(58) Ciucivara, A.; Sahu, B.; Kleinman, L. *Phys. Rev. B* **2007**, *76*, 064412.

(59) Fennie, C. J.; Ederer, C. J. *Phys.: Condens. Matter* **2008**, *20*, 434219.

(60) Pomjakushin, V. Yu.; Kenzelmann, M.; Doenni, A.; Harris, A. B.; Nakajima, T.; Mitsuda, S.; Tachibana, M.; Keller, L.; Mesot, J.; Kitazawa, H.; Takayama-Muromachi, E. *New J. Phys.* **2009**, *11*, 043019.

(61) Wang, L. J.; Chai, Y. S.; Feng, S. M.; Zhu, J. L.; Manivannan, N.; Jin, C. Q.; Gong, Z. Z.; Wang, X. H.; Li, L. T. *J. Appl. Phys.* **2012**, *111*, 114103.

(62) Chai, Y. S.; Oh, Y. S.; Wang, L. J.; Manivannan, N.; Feng, S. M.; Yang, Y. S.; Yan, L. Q.; Jin, C. Q.; Kim, K. H. *Phys. Rev. B* **2012**, *85*, 184406.